

# Intergranular precipitation-enhanced wetting and phase transformation in an Al<sub>0.4</sub>CoCrFeNi high-entropy alloy exposed to lead-bismuth eutectic

Xing Gong<sup>a,\*</sup>, Thierry Auger<sup>b</sup>, Wenjian Zhu<sup>a</sup>, Huasheng Lei<sup>c</sup>, Congying Xiang<sup>c</sup>, Zhiyang Yu<sup>c,\*</sup>, Michael P Short<sup>d</sup>, Pei Wang<sup>e</sup>, Yuan Yin<sup>a,\*</sup>

<sup>a</sup> *Advanced Nuclear Energy Research Team, Department of Nuclear Science and Technology, College of Physics and Optoelectronic Engineering, Shenzhen University, Shenzhen, 518060, China*

<sup>b</sup> *PIMM, Arts et Metiers ParisTech, CNRS, Cnam, HESAM Université, 151 Blvd. de L'Hôpital 75013 Paris, France*

<sup>c</sup> *State Key Laboratory of Photocatalysis on Energy and Environment, College of Chemistry, Fuzhou University, Fuzhou, 350002, China*

<sup>d</sup> *Department of Nuclear Science and Engineering, Massachusetts Institute of Technology (MIT), Cambridge, MA 02139, USA*

<sup>e</sup> *Additive Manufacturing Institute, College of Mechatronics and Control Engineering, Shenzhen University, Shenzhen, China*

*\*Corresponding authors*

*Email addresses: gongxing@szu.edu.cn (X. Gong); yuzyemlab@fzu.edu.cn (Z. Yu); yinyuan@szu.edu.cn (Y. Yin)*

## Abstract

After exposure to oxygen-poor ( $10^{-13} \sim 10^{-14}$  wt.%) liquid lead-bismuth eutectic (LBE) at 500°C for 500 h, LBE penetrates more than one order of magnitude deeper in an FCC Al<sub>0.4</sub>CoCrFeNi high-entropy alloy (HEA) decorated with a network of BCC (Ni, Al)-rich intergranular (IG) precipitates than in a single-phase, FCC Al<sub>0.3</sub>CoCrFeNi HEA without the IG precipitate network. This deterioration of corrosion resistance is attributed to the energetic nature of the BCC/FCC interphase boundaries (IBs) and resultant IB wetting. The LBE ingress film selectively leaches nickel located at those low-indexed crystalline planes, resulting in phase transformation from FCC to BCC structure.

*Keywords:* High entropy alloys; LBE; Corrosion; Wetting; Phase transformation

## **1. Introduction**

Liquid lead-bismuth eutectic (LBE,  $\text{Pb}_{44.5}\text{Bi}_{55.5}$ , wt. %) is a promising heat exchange fluid and spallation target material for Gen IV fast spectrum nuclear reactors, concentrated solar power systems (CSP), and accelerator driven systems (ADS), owing to its excellent thermophysical properties, inherent reactor safety, and high spallation neutron yield for ADS systems [1]. However, the deployment of these systems, typically designed using ferritic/martensitic (F/M) and/or austenitic stainless steels (AuSS), is still technically hampered by the degradation of these materials when brought into contact with LBE. These issues mostly include “liquid metal embrittlement” (LME) and “liquid metal corrosion” (LMC) [1, 2]. LME manifests itself as a strong reduction in ductility and toughness during mechanical loading in specific liquid metals. This effect occurs mainly in F/M steels exposed to LBE [3, 4], and can be mitigated by maintaining the service temperature above 450°C, where ductility starts to fully recover [5]. LMC can occur in both F/M steels and AuSS via oxidation, dissolution, locally-enhanced dissolution (also known as “pitting”), erosion, etc. [6-9]. To mitigate LMC, it is suggested to maintain the service temperature below 400°C [10]. Obviously, these two degradation mitigation strategies are mutually exclusive, and thus new materials with simultaneous resistance to LME and LMC are highly desirable.

High-entropy alloys (HEAs) may resolve this conundrum with their unique microstructures and promising properties [11-18]. This class of materials consist of at

least five nominally equimolar principal elements, thereby providing a wide compositional range for exploration. Among them, the  $\text{Al}_x\text{CoCrFeNi}$  type is one of the most investigated HEA systems, due to the ability to tailor their microstructures and mechanical properties by adjusting the Al content (i.e., as the Al content increases, the phase structure changes from pure FCC, FCC+BCC dual-phase to pure BCC) [19, 20]. In addition, the enriched Al enables to form a passivating alumina scale that can serve as an effective diffusion barrier against oxidative corrosion [21, 22]. In spite of good corrosion behavior, it was recently reported that one is not necessarily immune to LME [23], as evidenced with the dual-phase (FCC + BCC)  $\text{Al}_{0.7}\text{CoCrFeNi}$  (at. %) HEA in an oxygen-saturated LBE environment.

To further explore the degradation characteristics and associated mechanisms of the  $\text{Al}_x\text{CoCrFeNi}$ -series HEAs, we exposed an FCC-structured  $\text{Al}_{0.4}\text{CoCrFeNi}$  HEA decorated with a 3D network of BCC-structured (Ni, Al)-rich IG precipitates to oxygen-poor LBE at 500°C for 500 h. The results were compared with those obtained from a pure FCC  $\text{Al}_{0.3}\text{CoCrFeNi}$  HEA without the IG precipitate network. Remarkable differences in corrosion behavior were observed, with LBE penetration observed an order of magnitude deeper in the precipitate-laden HEA. A degradation mechanism is proposed based on detailed microstructural characterization using scanning electron microscopy (SEM) and scanning transmission electron microscope (STEM) equipped with a high angle annular dark field (HAADF) detector, which could aid in the design of future HEAs for applications in liquid metal cooled nuclear reactors.

## 2. Materials and experimental details

### 2.1 Materials

$\text{Al}_{0.3}\text{CoCrFeNi}$  and  $\text{Al}_{0.4}\text{CoCrFeNi}$  HEAs were fabricated by vacuum induction melting at  $1700^\circ\text{C}$ . To ensure homogeneity of chemical composition and microstructure, the HEAs were remelted/solidified four times. The cast ingots were then machined into discs with 12 mm in diameter and 3 mm in thickness for LBE exposure tests.

### 2.2 Exposure tests in LBE

The extremely poor oxygen condition was chosen to minimize the effect of surface oxidation on the intimate interactions between LBE and the HEA matrix, so that the intrinsic degradation mechanism can be explored. This conservative consideration is essential in the sense that protective surface oxide scales can be damaged somehow in service, which will lead to direct exposure of the HEA matrix to corrosive LBE, especially in crevices and occluded regions where dissolved oxygen could be very low. A schematic illustration of the exposure test apparatus and variation of the oxygen concentration dissolved in LBE during one of the exposures are presented in **Fig. 1**. The oxygen concentration dissolved in LBE was regulated by a self-developed oxygen controller which can automatically bubble oxygenated or hydrogenated gases into the LBE melt (**Fig. 1a**). During exposure, oxygen concentration was measured by potentiometric oxygen sensors with a LSC ( $\text{La}_{0.6}\text{Sr}_{0.4}\text{CoO}_3$ )/air reference electrode (**Fig. 1b**). The measured signal of the oxygen sensors was converted into oxygen concentration by means of the following equation [24]:

$$E = 0.6602 - 2.891 \cdot 10^{-4}T - 4.3086 \cdot 10^{-5}T \ln C_o \quad (1)$$

where  $E$  is the electromotive force (V) measured by the oxygen sensors;  $T$  is the temperature in Kelvin, and  $C_o$  is the oxygen concentration dissolved in LBE (wt. %).

### 2.3 Microstructure characterization

The two HEAs were cross-sectioned and polished to achieve a mirror-like surface finish, followed by electrochemical etching for 20 s in an oxalic acid solution (30 g oxalic acid dihydrate + 300 ml distilled water) at a DC voltage of 6~10 V. Afterwards, the original microstructure was examined by optical microscopy (Nikon, LV150 N) and SEM (ZEISS, Gemini 500). X-ray diffraction (XRD, Miniflex600) and TEM (Thermofisher Scientific Talos F200s, EDS system: 2 SDD windowless design, shutter-protected) were also used for phase identification.

After the LBE exposure tests, the specimens were polished with LBE residuals remaining on the surface using the same method described above. The polished cross-sections were examined under SEM to determine the structure of corrosion layers. FIB-SEM dual-beam microscope (Thermofisher Scientific Helios600i) was used to extract site-specific lamellae at LBE penetration tips for subsequent TEM and HAADF-STEM examination.

## 3. Results

### 3.1 Initial microstructure

The original microstructure of the  $Al_{0.3}CoCrFeNi$  and  $Al_{0.4}CoCrFeNi$  HEAs is presented in **Figs. 2** and **3a**, respectively. Both HEAs are characterized by equiaxed

grains with a mean grain size of about 150  $\mu\text{m}$  and a dominant austenite-like FCC phase (**Fig. 3b**). The major difference is that the grain boundaries (GBs) of the  $\text{Al}_{0.3}\text{CoCrFeNi}$  HEA are monophasic (**Fig. 2b**), while there exists a 3D network of BCC (Ni, Al)-rich IG precipitates (Co is also slightly enriched) at the GBs of the  $\text{Al}_{0.4}\text{CoCrFeNi}$  HEA (**Fig. 3c**). The GB precipitates have a thickness varying from less than one micron to a few microns. The TEM/EDS maps in **Fig. 3d** also show that numerous nanosized Cr-rich particles, the structure of which matches well with pure Cr (BCC), are dispersed inside the IG precipitates, and that the dominant FCC phase is rich in Co, Cr, Fe and Ni. Part of the FCC/BCC IBs are also decorated with those Cr-rich particles. The HRTEM (high-resolution TEM) image in **Fig. 3e** was recorded along the  $[111]_{\text{BCC}}//[110]_{\text{FCC}}$  direction, showing that the lattice from the BCC phase to the FCC phase are congruent and no evident misfit dislocations could be identified. This indicates that the FCC/BCC interphase boundary has a high degree of coherency. The corresponding FFT pattern in **Fig. 3f** identifies that the orientation relationship of these two phases is  $(10\bar{1})_{\text{BCC}}//(1\bar{1}\bar{1})_{\text{FCC}}$  and  $[111]_{\text{BCC}}//[110]_{\text{FCC}}$ . This coherency is understandable, as the lattice mismatch between the  $(10\bar{1})_{\text{BCC}}$  and  $(1\bar{1}\bar{1})_{\text{FCC}}$  crystallographic planes is small, i.e., around 0.5%, which could be accommodated by slight lattice distortion. Similarly, the interface between the Cr particle and the BCC IG precipitate phase shown in **Fig. 3g** is also coherent. The orientation relationship is  $(10\bar{1})_{\text{BCC}}//(10\bar{1})_{\text{Cr}}$  and  $[111]_{\text{BCC}}//[111]_{\text{Cr}}$ , as demonstrated by the corresponding FFT pattern in **Fig. 3h**. The total amount of IG precipitates is below the detectability threshold of XRD, so that their diffraction peaks are not present in **Fig. 3b**.

### *3.2 LBE ingress depth as a function of exposure times*

**Fig. 4** shows that the average LBE ingress depth at GBs of Al<sub>0.3</sub>CoCrFeNi HEA increases linearly with exposure time up to 500 h. Al<sub>0.4</sub>CoCrFeNi HEA exhibits a similar trend in the first 400 h of exposure, but the LBE penetration depth increases drastically from ~120 μm up to more than 3 mm within the final 100 h of exposure. It seems that an incubation period of about 400 h is required prior to the rapid LBE ingress, and a diffusion process of Pb and Bi atoms may dominate that incubation period.

### *3.3 Corrosion layers characterized by SEM/EDS*

**Fig. 5** compares the corrosion appearances of the two HEAs after the LBE exposures, showing remarkable differences. In the case of the single-phase Al<sub>0.3</sub>CoCrFeNi HEA, both transgranular dissolution (**Fig. 5a**) and LBE ingress at GBs (**Fig. 5b**) have occurred with a maximum corrosion depth of about 200 μm. Given this short depth of LBE ingress at the GBs, a GB grooving process driven by diffusion is more likely involved than a transition process due to GB wetting. By contrast, nearly the whole thickness (i.e., 3 mm) of the Al<sub>0.4</sub>CoCrFeNi HEA decorated with the 3D network of IG precipitation has been penetrated by LBE (**Fig. 5c**), leading to extraordinarily severe IG corrosion. Given such a large LBE ingress kinetics, liquid metal wetting must have occurred at the IG precipitation/matrix IBs. In addition, considering that elemental dissolution (e.g., Ni) takes place at the two sides of an LBE penetration tip and can to some extent widen the tip, the contact angle in **Fig. 5d** ends

up being not perfectly zero. At both sides of the prior GBs (**Fig. 5d**), the backscattered electrons (BSE) yield gives a different contrast from that of the matrix, suggesting that a new phase has been formed. This phase-transformed region does not include LBE, but instead rejects LBE to the surrounding matrix, meaning that both Pb and Bi are insoluble in the newly formed phase. The EDS line scan results presented in **Fig. 5e** reveal that the IG corrosion region is depleted in Ni, while Fe and Co are enriched mainly near the prior GB location (Al is also present). Moreover, the IG corrosion region contains Cr-rich phases. Except for some Al spikes, there is no obvious change in the Al content at the IG corrosion region in comparison to the matrix. Therefore, the corrosion products are composed mainly of a (Fe, Co, Al)-rich phase and Cr-rich phases, while the prior BCC-structured (Ni, Al)-rich IG precipitates have been destroyed by LBE.

### *3.4 TEM characterization on LBE penetration tip of $Al_{0.3}CoCrFeNi$ HEA*

The microstructure characteristics at a LBE penetration tip in the  $Al_{0.4}CoCrFeNi$  HEA after exposure to oxygen-poor LBE at 500°C for 400 h is presented in **Fig. 6**. It can be seen that a corrosion product is formed at the prior GB area (**Fig. 6a**). Cr is depleted in the corrosion product since this element is slightly soluble in oxygen-depleted LBE with a solubility of ~10.7 ppm at 500°C, while the other constituting elements are also lower than the matrix (**Fig. 6b**). Note that the highly soluble element Ni is visible at this area. This may result from recondensation of LBE-dissolved Ni. **Fig. 6c** shows that the corrosion product/LBE and HEA matrix/LBE interfaces are faceted,

mostly following certain low-indexed crystallographic planes, such as {221}, {112}, {022} and {111}. The selected area electron diffraction (SAED) pattern identifies that the corrosion product has a ferrite-like structure. This suggests that phase transformation has occurred at the LBE penetration tip.

### *3.5 TEM characterization on LBE penetration tip of Al<sub>0.4</sub>CoCrFeNi HEA*

The corrosion products in Al<sub>0.4</sub>CoCrFeNi HEA are more complex, as shown in **Figs. 7 and 8**. **Fig. 7a** is a HAADF-STEM image taken from an electron-transparent lamella prepared by FIB lift-out at an LBE ingress tip in the Al<sub>0.4</sub>CoCrFeNi HEA after the LBE exposure. The two areas marked with “I” and “II” are corrosion products. The EDS maps in **Fig. 7b** show that Co, Fe, and Al are the major constituents of the corrosion products, while Cr and Ni are depleted in those two areas, except for the presence of a few Cr-rich particles and many (Ni, Al, Co)-rich strips. The magnified view of region “I” and the corresponding EDS maps in **Figs. 7c and 7d** show (Ni, Al, Co)-rich strips more clearly. Such strips are also present in the Cr-rich particles (**Figs. 7e and 7f**). Pb and Bi are not detected in the whole tip area. The interfaces of LBE and IG corrosion products are faceted and mostly prone to follow certain low-indexed crystallographic planes (**Figs. 8a and 8b**), identified here as {111}, {002} and {112}. The interfaces between the HEA matrix and LBE are also faceted, following planes such as {111} and {220}, see **Fig. 8c**. Similar to Al<sub>0.3</sub>CoCrFeNi HEA, the SAED patterns and HRTEM images in **Figs. 8a and 8b** match well with the BCC ferrite structure (PDF #54-0331), indicating that a phase transformation from the initial austenite-like FCC structure to a

ferrite-like BCC structure has occurred at the IG corrosion region of Al<sub>0.4</sub>CoCrFeNi HEA. The faceting could then result from the equilibrium between the interfacial energetics of various solid-liquid orientations.

#### 4. Discussion

Exposure of a solid metal to a liquid metal leads to formation of grooves at GBs of the solid metal. After a thermodynamic equilibrium is reached, the balance among the interfacial energies can be described by the following equation [25]:

$$(\gamma_{sl}^1 + \gamma_{sl}^2) \cdot \cos(\theta/2) = \gamma_{gb} \quad (2)$$

where  $\gamma_{sl}^1$ ,  $\gamma_{sl}^2$  and  $\gamma_{gb}$  are the interfacial energies of the two solid metal/liquid metal interfaces and a GB, respectively, and  $\theta$  is the dihedral angle at the triple line. Above a certain transition temperature, one reaches the new condition:  $(\gamma_{sl}^1 + \gamma_{sl}^2) \leq \gamma_{gb}$ , in this case, GB wetting can occur with  $\theta$  dropping to zero and the liquid metal can spontaneously penetrate into GBs. The energy difference between  $\gamma_{gb}$  and  $(\gamma_{sl}^1 + \gamma_{sl}^2)$ , defines the driving force and kinetics for GB wetting. Typical GB wetting cases include Al/Ga [26, 27], Cu/Bi [28, 29], Ni/Bi [30, 31], Mo/Ni [32], steels/Zn [33-36], etc. Obviously, the Al<sub>0.4</sub>CoCrFeNi/LBE system is a new one, in which liquid metal wetting occurs at the FCC/BCC IBs (i.e.,  $\gamma_{sl}^1 + \gamma_{sl}^2 \leq \gamma_{IB}$ , where  $\gamma_{IB}$  is the interfacial energy of FCC/BCC IBs). Interestingly, wetting does not actively occur at the pure FCC GBs of the Al<sub>0.3</sub>CoCrFeNi HEA (**Fig. 5b**), although the chemical compositions of these two HEAs are very close. This difference in wetting behavior can be ascribed to their differing microstructural boundary structures. From energy point of view, it is also

suggested that the FCC/BCC interphase is more energetically favorable for LBE wetting than the FCC/FCC grain boundary.

At 500°C, the solubility limit of Ni in LBE is about 27,504 ppm, while Cr and Fe have a solubility limit of only 10.7 ppm and 2.2 ppm, respectively [37]. After IBs are wetted by LBE, therefore, the highly soluble element Ni is selectively leached out from the matrix at the lateral sides of the IBs, resulting in phase transformation from the initial austenite-like FCC structure to a ferrite-like BCC structure (**Figs. 8a and 8b**). This new phase appears dense and seems to differ from the phase transformation from FCC austenite to BCC ferrite in AuSS induced by leaching of Ni which is an austenite stabilizer. In the latter case, a volume expansion of 1.19% and many LBE-filled micropores are produced in the ferritization zones [9, 38]. By contrast, the new phase formed in the  $Al_{0.4}CoCrFeNi$  HEA is relatively dense and immiscible with LBE, so that LBE segregates and forms a very narrow path for the mass transfer of the leached species (**Fig. 5d**). In addition, it is worthwhile noting that the leaching of Ni from the matrix as LBE penetration proceeds will change the chemical composition of the surface layers in contact with LBE, leading to reduction of the entropy at that area. It is challenging, however, to quantify the relationship between the high entropy core effect and LBE penetration.

Based on the discussion above, a qualitative mechanism regarding the corrosion process of the  $Al_{0.4}CoCrFeNi$  HEA exposed to oxygen-poor LBE at 500°C can be schematically illustrated in **Fig. 9**. When the  $Al_{0.4}CoCrFeNi$  HEA with a 3D network of BCC (Ni, Al)-rich IG precipitates is exposed to LBE (**Fig. 9a**), LBE wets the IB most

likely due to the favorable energetics (**Fig. 9b**). Then, the highly soluble element Ni is selectively leached out, not only from the matrix, but also from the Ni-rich IG precipitates. The leached Ni stays in LBE until its saturation is reached, and then is transferred to the external LBE pool (**Fig. 9c**). The leaching leads to the phase transformation from the initial austenite-like FCC structure to a ferrite-like BCC structure, and the IG corrosion area increases as the leaching front advances (**Fig. 9d**). The leaching process takes place preferentially at low-indexed crystallographic planes, and injects vacancies and microvoids in place of Ni atoms, probably enhancing diffusion and so the leaching process (**Fig. 9e**). GB grooving by Pb and Bi probably accelerates as well the leaching process at the front. Since the IG corrosion products resulting from the elemental leaching are dense and immiscible with LBE, LBE is pushed to the matrix side. Finally, the IG corrosion products are mainly composed of a BCC, (Fe, Co, Al)-rich phase, and of Cr-rich particles. The formation of the latter results from either atomic rearrangement of the Cr atoms in the leaching-disrupted HEA lattice or it grows from the pre-existing nanosized Cr-rich particles in the IG precipitates.

## 5. Conclusions

In summary, the presence of BCC (Ni, Al)-rich IG precipitation containing numerous nanosized Cr-rich particles makes the  $\text{Al}_{0.4}\text{CoCrFeNi}$  HEA very sensitive to LBE wetting at  $500^\circ\text{C}$ . The fast LBE ingress along the IBs is accompanied by severe leaching of Ni, leading to the phase transformation from an initial austenite-like FCC structure to a ferrite-like BCC structure. It can be expected that this corrosion

mechanism will bring about a serious LME issue when tensile stress is applied, as the cohesion of the IBs is greatly weakened by the LBE ingress. The results obtained in this work suggest strongly that the presence of the heterogeneous IBs is a critical performance-limiting factor for applications in LBE environments (and perhaps those involving other highly wetting fluids) at elevated temperatures, and the future HEAs designs should minimize the amount of any heterogeneous boundary networks.

### **Acknowledgements**

X.G. thanks the financial support from the National Natural Science Foundation of China (Grant No. 51801129). M.P.S. acknowledges funding received from the United States Department of Energy (DOE) Office of Nuclear Energy's Nuclear Energy University Program (NEUP) (Grant No. DE-NE0008871).

### **Data availability statement**

Most of the raw/processed data required to reproduce these findings have been presented in this paper. More details about the raw data can be shared upon request.

### **Declaration of interests**

The authors declare that they have no known competing financial interests or personal relationships that could have appeared to influence the work reported in this paper.

## References

- [1] OECD/NEA, Handbook on lead-bismuth eutectic alloy and lead properties, materials compatibility, thermal-hydraulics and technologies, 2015.
- [2] X. Gong, R. Li, M.Z. Sun, Q.S. Ren, T. Liu, M.P. Short, *J Nucl. Mater.* 482 (2016) 218-228.
- [3] D. Gorse, T. Auger, J.-B. Vogt, I. Serre, A. Weisenburger, A. Gessi, P. Agostini, C. Fazio, A. Hojná, F. Di Gabriele. *J Nucl. Mater.* 415 (2011) 284-292.
- [4] A. Hojná, P. Halodová, M. Chocholoušek, Z Špirit, L. Rozumová. *Corros. Rev.* 38 (2020) 183-194.
- [5] B. Long, Y. Dai, N. Baluc. *J Nucl. Mater.* 431 (2012) 85-90.
- [6] V. Tsisar, C. Schroer, O. Wedemeyer, A. Skrypnik, J. Konys. *J Nucl. Mater.* 468 (2016) 305-312.
- [7] K. Lambrinou, E. Charalampopoulou, T. Van der Donck, R. Delville, D. Schryvers. *J Nucl. Mater.* 490 (2017) 9-27.
- [8] K. Lambrinou, V. Koch, G. Coen, J. Van den Bosch, C. Schroer. *J Nucl. Mater.* 450 (2014) 244-255.
- [9] P. Hosemann, D. Frazer, E. Stergar, K. Lambrinou. *Scripta Mater.* 118 (2016) 37-40.
- [10] A. Aerts, K. Gladinez, B. Gonzalez Prieto, J. Lim, A. Marino, K. Rosseel. *Proc. 14th Int. Workshop on Spallation Materials Technology, JPS Conf. Proc.* 28 (2020) 071002.
- [11] E.P. George, W.A. Curtin, C.C. Tasan, *Acta Mater.* 188 (2020) 435-474.
- [12] Z.Z. Li, S.T. Zhao, R.O. Ritchie, M.A. Meyers, *Prog. in Mater. Sci.* 102 (2019) 296-345.
- [13] P. Sathiyamoorthi, H.S. Kim. *Prog. in Mater. Sci.* 123 (2022) 100709.

- [14] K. Biswas, J.-W. Yeh, P. P. Bhattacharjee, J. Th. M. DeHosson. *Scripta Mater.* 188 (2020) 54-58.
- [15] M.P. Agustianingrum, S.H. Yoshida, N. Tsuji, N. Park. *J. Alloys Comp.* 781 (2019) 866-872.
- [16] H. Kim, D. Lee, H. Kim, Y. Kim, M. Jang, D. Kwen, Y. Koo, E. Kim, H. Cho, M.P. Agustianingrum, N. Park, B. Straumal. *Mater. Lett.* 303 (2021) 130481.
- [17] M.P. Agustianingrum, U. Lee, N. Park. *Corros. Sci.* 173 (2020) 108755.
- [18] M.P. Agustianingrum, F. H. Latief, N. Park, U. Lee. *Intermetallics*, 120 (2020) 106757.
- [19] W.R. Wang, W.L. Wang, S.C. Wang, Y.C. Tsai, C.H. Lai, J.W. Yeh. *Intermetallics*, 26 (2012) 44-51.
- [20] J.C. Rao, H.Y. Diao, V. Ocelík, D. Vainchtein, C. Zhang, C. Kuo, Z. Tang, W. Guo, J.D. Poplawsky, Y. Zhou, P.K. Liaw, J. Th. M. De Hosson. *Acta Mater.* 131 (2017) 206-220.
- [21] J. Lu, Y. Chen, H. Zhang, L. Li, L.M. Fu, X.F. Zhao, F.W. Guo, P. Xiao. *Corros. Sci.* 170 (2020) 108691.
- [22] H. Shi, A. Jianu, R. Fetzer, D.V. Szabó, S. Schlabach, A. Weisenburger, C.C. Tang, A. Heinzl, F.B. Lang, G. Müller, *Corros. Sci.* 189 (2021) 109593.
- [23] X. Gong, C.Y. Xiang, T. Auger, J.J. Chen, X.C. Liang, Z.Y. Yu, M.P. Short, M. Song, Y. Yin. *Scripta Mater.* 194 (2021) 113652.
- [24] G. Manfredi, J. Lim, K. Rosseel, J. Van den Bosch, T. Doneux, C. Buess-Herman, A. Aerts. *Sens. Actuators B* 214 (2015) 20-28.
- [25] J. Luo. *Corros.* 72 (2016) 897-910.
- [26] E. Pereiro-Lopez, W. Ludwig, D. Bellet, P. Cloetens, C. Lemaignan, *Phys. Rev. Lett.* 95 (2005) 215501.

- [27] M. Shen, Y. Li, C. Hu, S. Xue, C. Xiang, J. Luo, Z. Yu, The interfacial structure underpinning the Al-Ga liquid metal embrittlement: disorder vs. order gradients. *Scripta Mater.* 204 (2021) 114149.
- [28] A. Kundu, K.M. Asl, J. Luo, M.P. Harmer, *Scripta Mater.* 68 (2013) 146-149.
- [29] G. Duscher, M. F. Chisholm, U. Alber, M. Rühle, *Nat. Mater.* 3 (2004) 621-626.
- [30] J. Luo, H. Cheng, K.M. Asl, C.J. Kiely, M.P. Harmer. *Science*, 333 (2011) 1730-1733.
- [31] Z.Y. Yu, P.R. Cantwell, Q. Gao, D. Yin, Y.Y. Zhang, N.X. Zhou, G.S. Rohrer, M. Widom, J. Luo, M.P. Harmer. *Science*, 358 (2017) 97-101.
- [32] X.M. Shi, J. Luo, *Appl. Phys. Lett.* 94 (2009) 251908.
- [33] L. Cho, H. Kang, C. Lee, B.C. De Cooman, *Scripta Mater.* 90 (2014) 25-28.
- [34] R. Ashiri, M. Shamanian, H.R. Salimijazi, MA Haque, J.H. Bae, C.W. Ji, K.G. Chin, Y.D. Park. *Scripta Mater.* 114 (2016) 41-47.
- [35] R. Ashiri, M.A. Haque, C.W. Ji, M. Shamanian, H.R. Salimijazi, Y.D. Park. *Scripta Mater.* 109 (2015) 6-10.
- [36] D. Bhattacharya, L. Cho, E. van der Aa, H. Ghassemi-Armaki, A. Pichler, K.O. Findley, J.G. Speer. *Scripta Mater.* 175 (2020) 49-54.
- [37] J.S. Zhang, N. Li, *J Nucl. Mater.* 373 (2008) 351-377.
- [38] X. Gong, Z.B. Yang, Y.B. Deng, J. Xiao, H. Wang, Z.Y. Yu, Y. Yin. *Mater. Sci. Eng. A*, 798 (2020) 140230.

## Figure captions

**Fig. 1.** (a) Schematic illustration of the LBE exposure apparatus and (b) the variation of oxygen concentration dissolved in LBE during an exposure test. The error of the temperature measurements is about  $\pm 2^\circ\text{C}$ .

**Fig. 2.** SEM micrographs of original microstructure of the  $\text{Al}_{0.3}\text{CoCrFeNi}$  HEA, showing that no IG precipitates exist at GBs. (a)  $\times 500$ ; (b)  $\times 1000$ .

**Fig. 3.** Original microstructure of the  $\text{Al}_{0.4}\text{CoCrFeNi}$  HEA: (a) Optical micrograph, (b) XRD pattern, (c) Backscattered electron (BSE)-SEM image of IG precipitates, (d) TEM/EDS maps of the IG precipitates, (e) HRTEM (high-resolution TEM) image of the FCC/BCC IB and (f) the corresponding FFT (fast Fourier transform) pattern, (g) HRTEM image of a Cr-rich nanoparticle/BCC interface and (h) the corresponding FFT pattern.

**Fig. 4.** Comparison of average LBE ingress depth at GBs of  $\text{Al}_{0.3}\text{CoCrFeNi}$  and  $\text{Al}_{0.4}\text{CoCrFeNi}$  HEAs as a function of exposure times.

**Fig. 5.** Backscattered electron (BSE)-SEM images of the corrosion appearances in the single-phase FCC  $\text{Al}_{0.3}\text{CoCrFeNi}$  (a, b) and the IG precipitate-decorated FCC  $\text{Al}_{0.4}\text{CoCrFeNi}$  (c, d) after exposure to the oxygen-poor ( $10^{-13} \sim 10^{-14}$  wt. %) LBE at  $500^\circ\text{C}$  for 500 h. Both transgranular dissolution and LBE ingress at GBs occur in the single-phase  $\text{Al}_{0.3}\text{CoCrFeNi}$  HEA, and the maximum corrosion depth is about  $200\ \mu\text{m}$ , while the whole thickness of the IG precipitate-decorated  $\text{Al}_{0.4}\text{CoCrFeNi}$  HEA specimen was penetrated by LBE with a very small wetting angle of  $\sim 0^\circ$  at the IB (d), forming a network of IG corrosion regions with complex chemical compositions (e).

**Fig. 6.** HAADF-STEM images (a, c), EDS maps (b) and SAED patterns of an LBE penetration tip at a GB of  $\text{Al}_{0.3}\text{CoCrFeNi}$  HEA after exposure to oxygen-poor LBE at

500°C for 400 h. It is shown that the corrosion product is depleted in Cr and has a ferrite-like structure (BCC). Both the corrosion product/LBE interfaces and matrix/LBE interfaces are faceted.

**Fig. 7.** HAADF-STEM image (a) and corresponding EDS maps (b) of an LBE penetration tip at an IG precipitate/matrix boundary of  $\text{Al}_{0.4}\text{CoCrFeNi}$  HEA after exposure to oxygen-poor LBE at 500°C for 500 h (the corrosion products are marked with “I” and “II”); (c) a magnified HAADF-STEM image and EDS maps (d) of the corrosion product “I”; (e, f) (Ni, Al, Co)-rich strips exist in Cr particles in the corrosion product “I”.

**Fig. 8.** (a) HRTEM image of the LBE/corrosion product (“I”) interface and SAED pattern of the corrosion product (“I”) in **Fig. 7a**; (b) TEM bright-field (BF) image and SAED pattern of the corrosion product (“II”) in **Fig. 7a**; (c) TEM-BF image and SAED pattern at the LBE/matrix interface. The tested sample was  $\text{Al}_{0.4}\text{CoCrFeNi}$  HEA exposed to oxygen-poor LBE at 500°C for 500 h.

**Fig. 9.** Schematic illustration of the corrosion process of  $\text{Al}_{0.4}\text{CoCrFeNi}$  HEA exposed to oxygen-poor LBE at 500°C. An initially closed IB (a) begins to open by perfect LBE wetting (b), allowing the highly soluble element Ni to be leached out from the matrix and the Ni-rich IG precipitates. The leached Ni remains in LBE until its saturation is reached, and then is transferred to the external LBE (c). The leaching leads to formation of LBE-immiscible corrosion products that have a crystalline structure similar to ferrite (d). (e) shows a zoomed-in atomic-level view at the leaching front. The corrosion products are mainly composed of an (Fe, Co, Al)-rich phase (a ferrite-like BCC structure) and Cr-rich particles, with dispersion of numerous (Ni, Al, Co)-rich strips.

## Figures

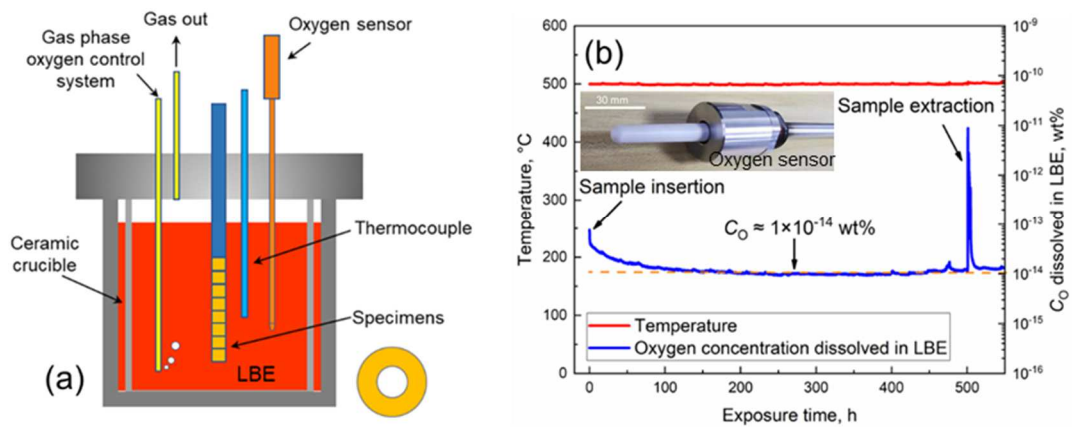


**Fig. 1.** (a) Schematic illustration of the LBE exposure apparatus and (b) the variation of oxygen concentration dissolved in LBE during an exposure test. The error of the temperature measurements is about  $\pm 2^\circ\text{C}$ .

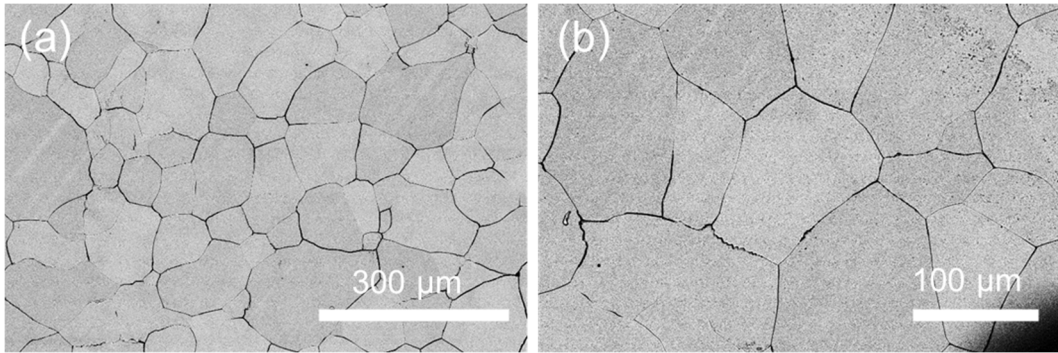


**Fig. 2.** SEM micrographs of original microstructure of the  $\text{Al}_{0.3}\text{CoCrFeNi}$  HEA, showing that no IG precipitates exist at GBs. (a)  $\times 500$ ; (b)  $\times 1000$ .

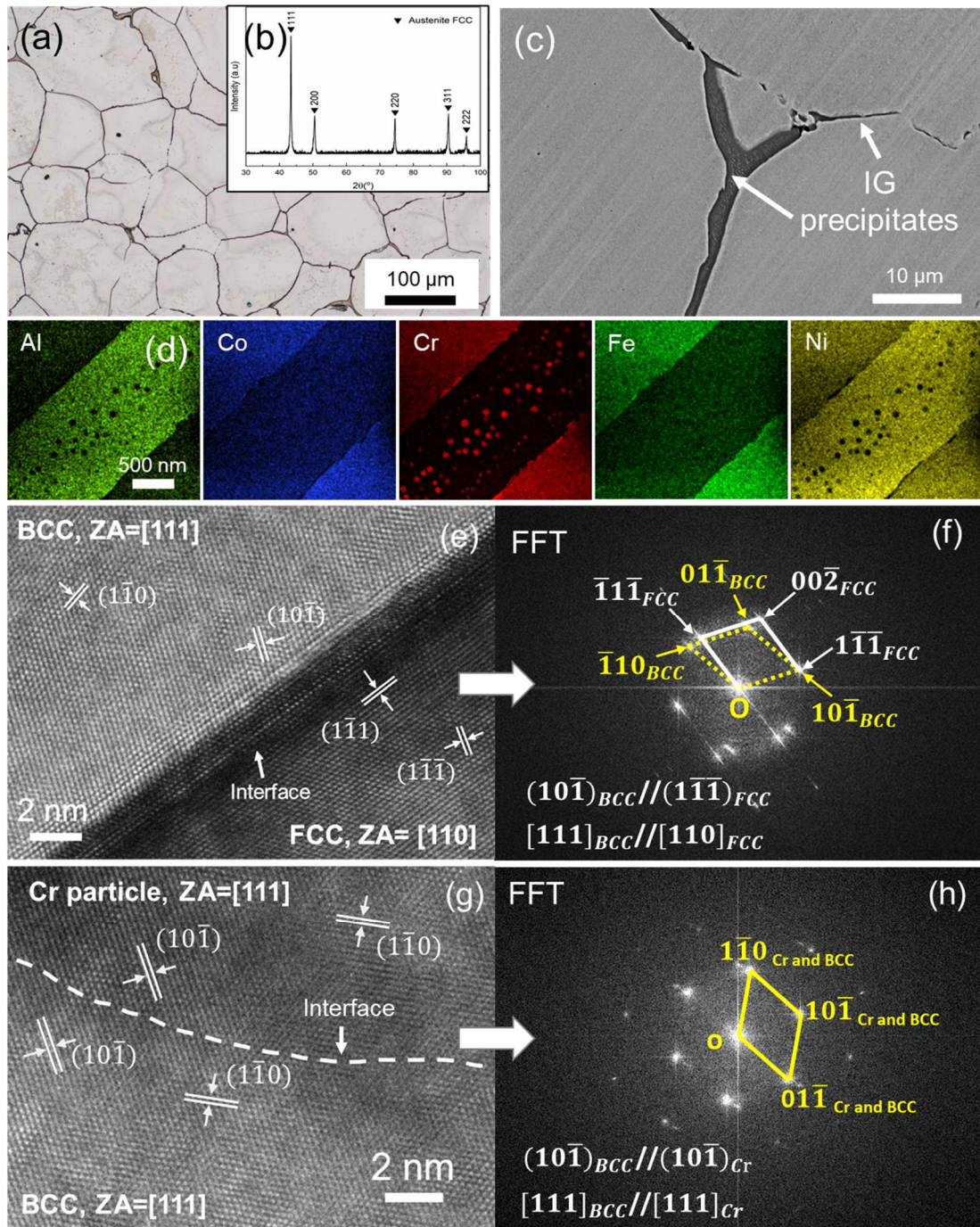


**Fig. 3.** Original microstructure of the  $\text{Al}_{0.4}\text{CoCrFeNi}$  HEA: (a) Optical micrograph, (b) XRD pattern, (c) Backscattered electron (BSE)-SEM image of IG precipitates, (d) TEM/EDS maps of the IG precipitates, (e) HRTEM (high-resolution TEM) image of the FCC/BCC IB and (f) the corresponding FFT (fast Fourier transform) pattern, (g) HRTEM image of a Cr-rich nanoparticle/BCC interface and (h) the corresponding FFT pattern.

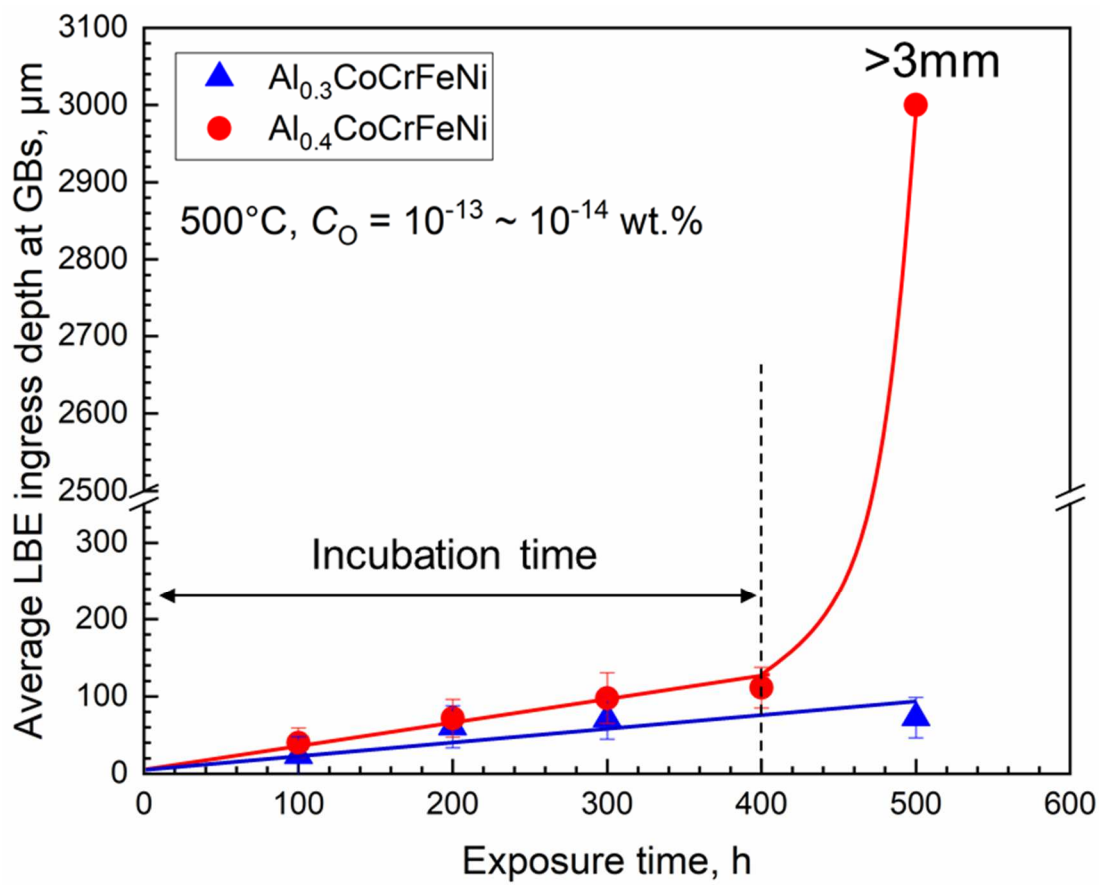


**Fig. 4.** Comparison of average LBE ingress depth at GBs of Al<sub>0.3</sub>CoCrFeNi and Al<sub>0.4</sub>CoCrFeNi HEAs as a function of exposure times.

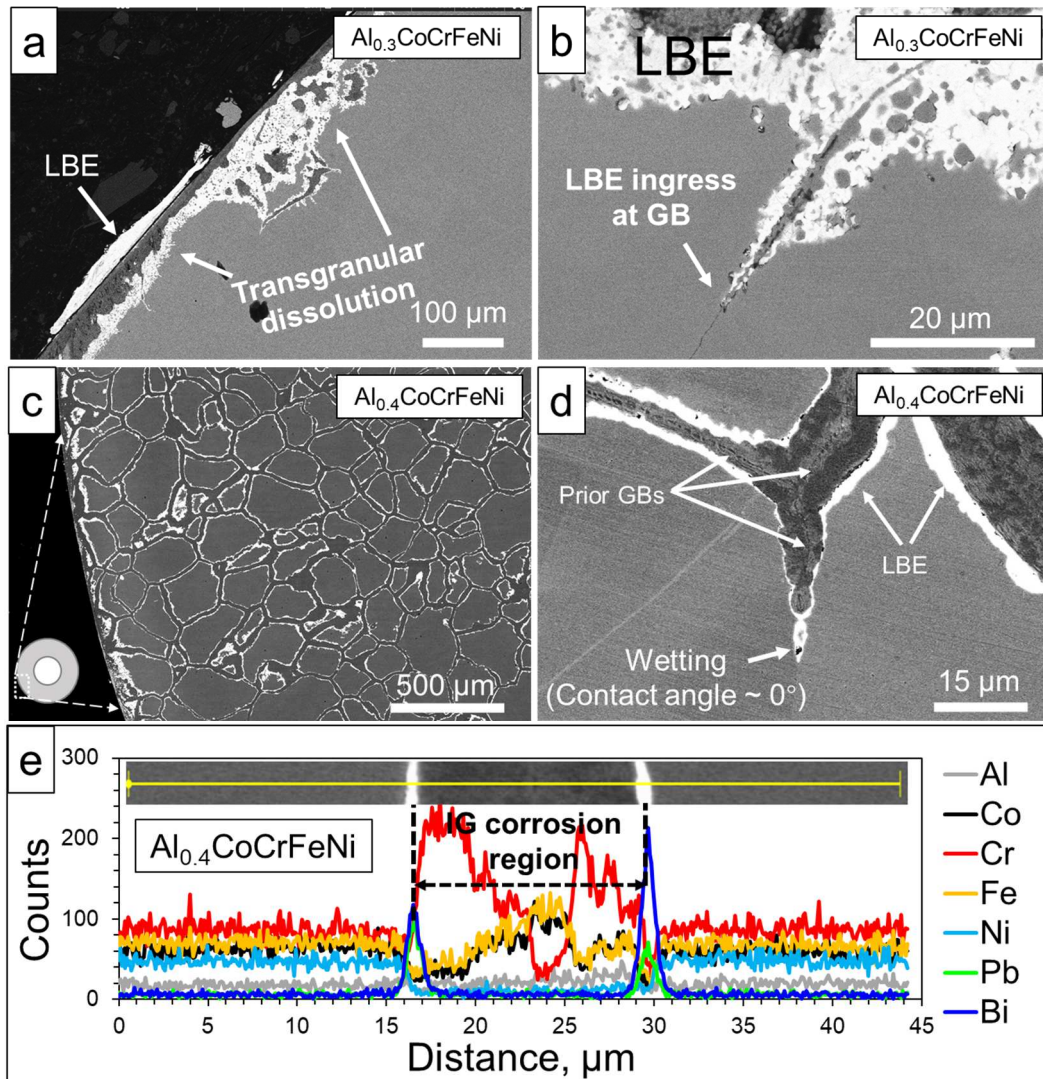


**Fig. 5.** Backscattered electron (BSE)-SEM images of the corrosion appearances in the single-phase FCC  $\text{Al}_{0.3}\text{CoCrFeNi}$  (a, b) and the IG precipitate-decorated FCC  $\text{Al}_{0.4}\text{CoCrFeNi}$  (c, d) after exposure to the oxygen-poor ( $10^{-13} \sim 10^{-14}$  wt. %) LBE at  $500^\circ\text{C}$  for 500 h. Both transgranular dissolution and LBE ingress at GBs occur in the single-phase  $\text{Al}_{0.3}\text{CoCrFeNi}$  HEA, and the maximum corrosion depth is about  $200 \mu\text{m}$ , while the whole thickness of the IG precipitate-decorated  $\text{Al}_{0.4}\text{CoCrFeNi}$  HEA specimen was penetrated by LBE with a very small wetting angle of  $\sim 0^\circ$  at the IB (d), forming a network of IG corrosion regions with complex chemical compositions (e).

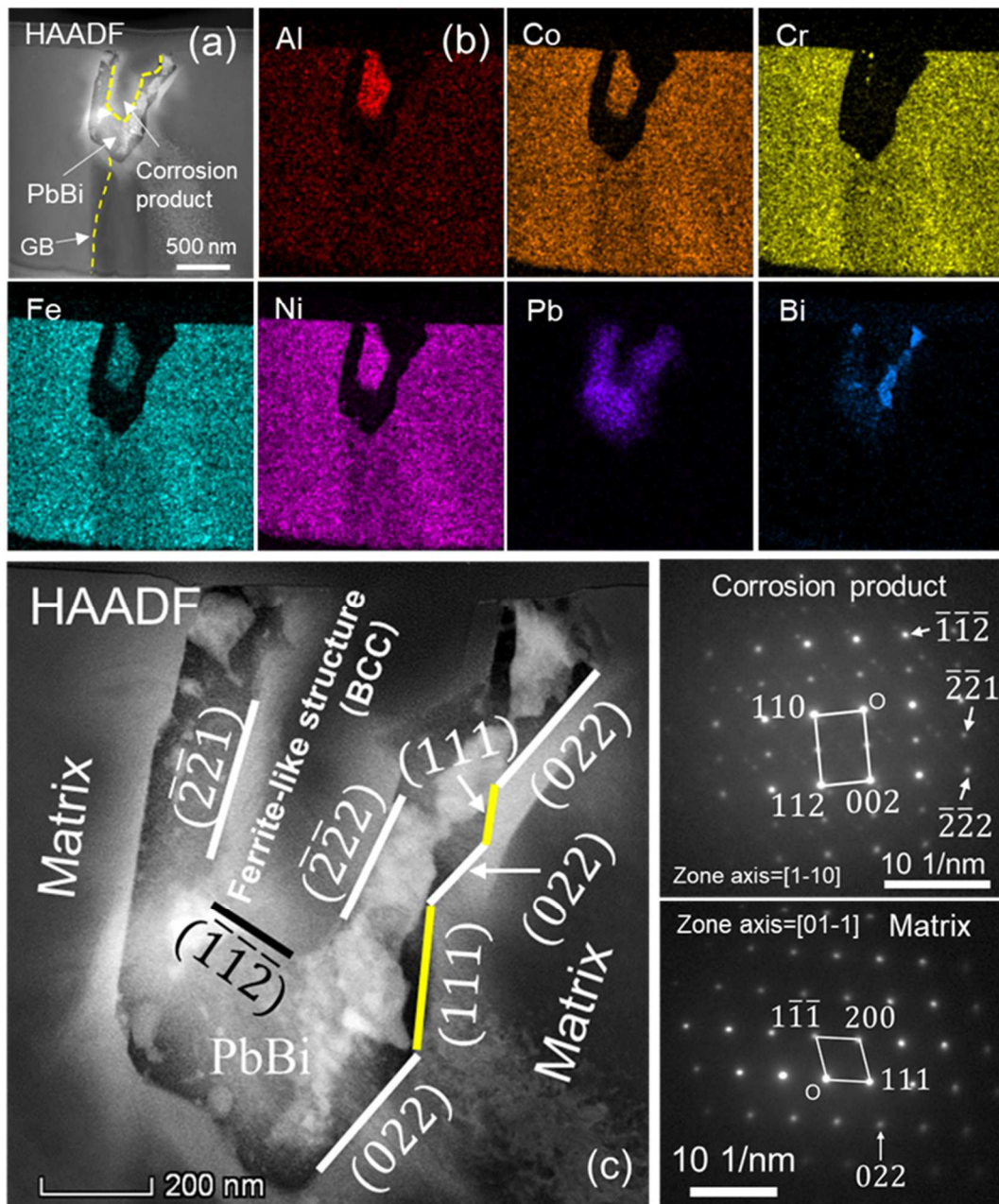


**Fig. 6.** HAADF-STEM images (a, c), EDS maps (b) and SAED patterns of an LBE penetration tip at a GB of  $\text{Al}_{0.3}\text{CoCrFeNi}$  HEA after exposure to oxygen-poor LBE at  $500^\circ\text{C}$  for 400h. It is shown that the corrosion product is depleted in Cr and has a ferrite-like structure (BCC). Both the corrosion product/LBE interfaces and matrix/LBE interfaces are faceted.

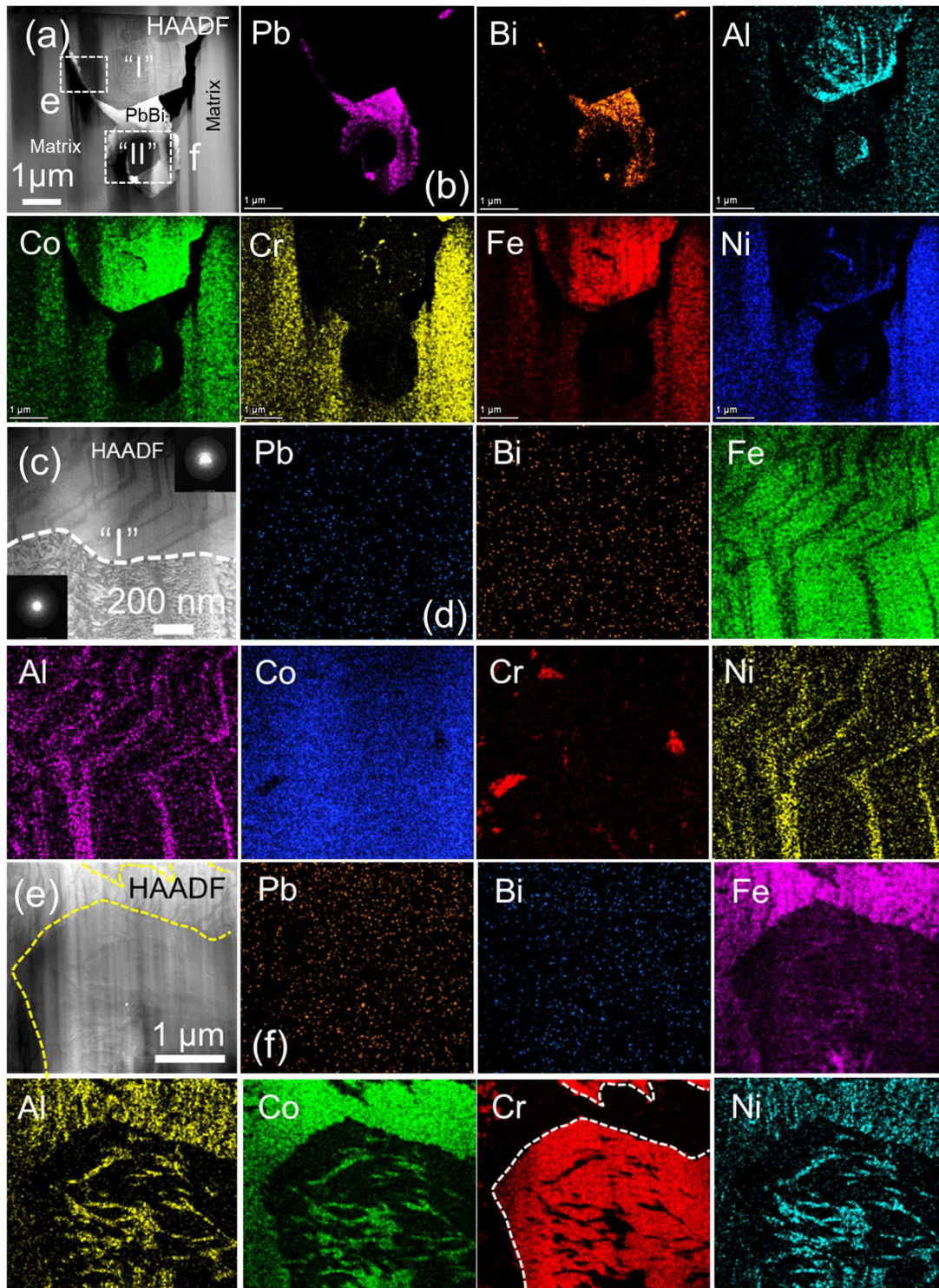


**Fig. 7.** HAADF-STEM image (a) and corresponding EDS maps (b) of an LBE penetration tip at an IG precipitate/matrix boundary of  $\text{Al}_{0.4}\text{CoCrFeNi}$  HEA after exposure to oxygen-poor LBE at  $500^\circ\text{C}$  for 500 h (the corrosion products are marked with “I” and “II”); (c) a magnified HAADF-STEM image and EDS maps (d) of the corrosion product “I”; (e, f) (Ni, Al, Co)-rich strips exist in Cr particles in the corrosion product “I”.

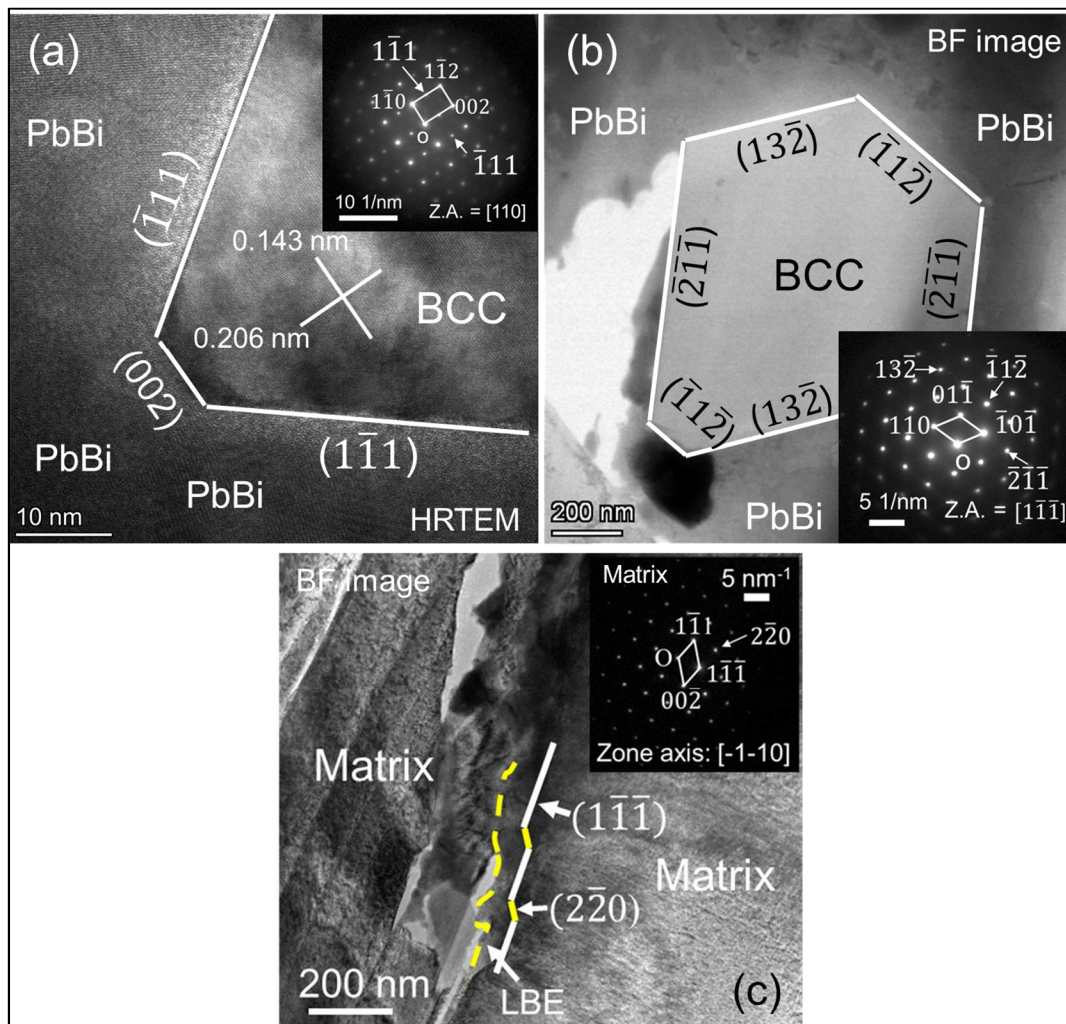


**Fig. 8.** (a) HRTEM image of the LBE/corrosion product (“I”) interface and SAED pattern of the corrosion product (“I”) in Fig. 7a; (b) TEM bright-field (BF) image and SAED pattern of the corrosion product (“II”) in Fig. 7a; (c) TEM-BF image and SAED pattern at the LBE/matrix interface. The tested sample was Al<sub>0.4</sub>CoCrFeNi HEA exposed to oxygen-poor LBE at 500°C for 500 h.

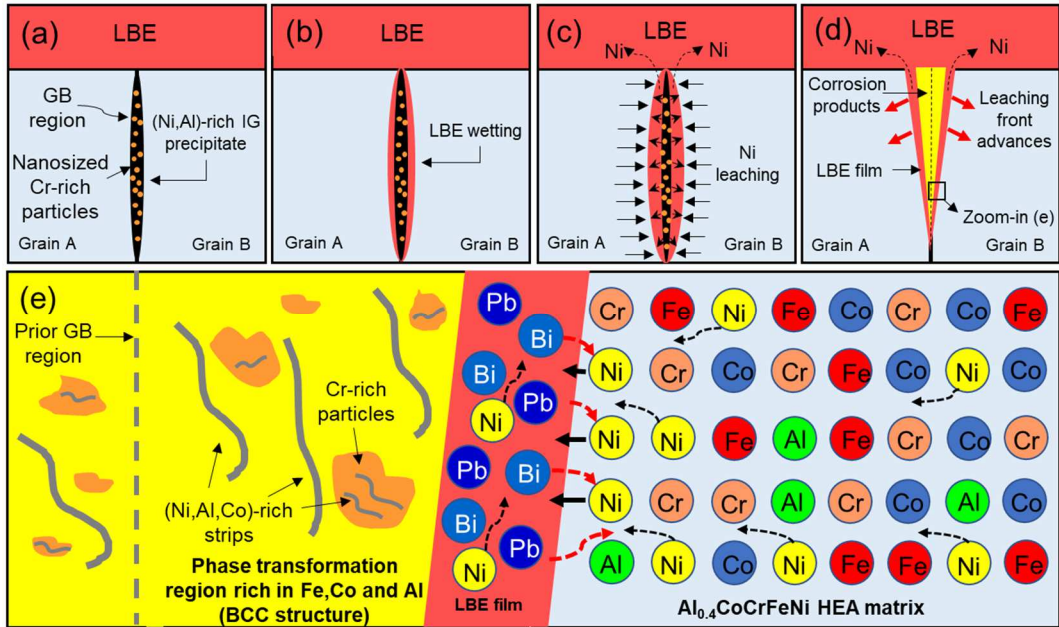


**Fig. 9.** Schematic illustration of the corrosion process of  $\text{Al}_{0.4}\text{CoCrFeNi}$  HEA exposed to oxygen-poor LBE at  $500^\circ\text{C}$ . An initially closed IB (a) begins to open by perfect LBE wetting (b), allowing the highly soluble element Ni to be leached out from the matrix and the Ni-rich IG precipitates. The leached Ni remains in LBE until its saturation is reached, and then is transferred to the external LBE (c). The leaching leads to formation of LBE-immiscible corrosion products that have a crystalline structure similar to ferrite (d). (e) shows a zoomed-in atomic-level view at the leaching front. The corrosion products are mainly composed of an (Fe, Co, Al)-rich phase (a ferrite-like BCC structure) and Cr-rich particles, with dispersion of numerous (Ni, Al, Co)-rich strips.